WILEY | Hindawi

Research Article

A Baseline-Free Lamb Wave Damage Localization Method Based on Compressed Sensing

Xiushi Cui [iD],[1] **Bo Song,**[2] **Dongsheng Li** [iD],[1] **and Jiahe Liu** [iD][1]

[1]*State Key Laboratory of Coastal and Offshore Engineering, Dalian University of Technology, Dalian, Liaoning Province 116024, China*
[2]*School of Marine Technology and Environment, Dalian Ocean University, Dalian, Liaoning Province 116023, China*

Correspondence should be addressed to Dongsheng Li; lidongsheng@dlut.edu.cn

In conventional Lamb wave-based damage detection, estimation is generally performed using the difference between the measured and baseline signals. However, it is difficult to maintain consistent measurement conditions between the measured and baseline signals, likely leading to large measurement errors. This paper proposed a baseline-free Lamb wave-based detection method for locating damage to structures. The damage scattering waves are extracted according to their features in the frequency-wavenumber spectrum and the damage locations are visualized using probability imaging. To reduce the complications of full wavefield acquisition, wavefield data are acquired using piezoelectric transducer (PZT) arrays at sampling rates much lower than the Nyquist frequency, and the original wavefield is reconstructed by applying compressed sensing. Experimental results on an aluminum plate indicate that the proposed method can provide the damage probability at each plate position without requiring a reference signal, suggesting its applicability to damage diagnosis of structures. Moreover, the proposed method achieves a compression ratio of 86.7% compared with the use of Nyquist sampling.

1. Introduction

In research on plate and shell structure detection, using Lamb waves is a promising approach owing to their long-distance propagation, small blind area, and other advantages. Lamb waves interact with damage in a medium, resulting in transmission, scattering, and reflection, which in turn change the amplitude and phase of the original signal and generate damage scattering waves. Therefore, Lamb waves carry representative information about structural damage, and structural health can be evaluated by analyzing the acquired signal characteristics.

Owing to the dispersion and multimode properties of Lamb waves, damage scattering waves are easily confused by boundary-reflection waves, non-target-mode waves, and environmental noise [1]. Most current methods for Lamb wave-based damage detection use a nondestructive test signal as a baseline, and the damage scattering wave is obtained by subtraction from the damage signal. Huo et al.

[2] proposed a Bayesian damage imaging method based on the reconstruction algorithm for the probabilistic inspection of defects (RAPIDs), which performs accurate structural damage imaging of composite materials. Liu et al. [3] modeled composite materials with propagation velocity anisotropy and used probability imaging to evaluate structural damage. Yuan et al. [4] developed the multiple signal classification (MUSIC) algorithm for damage localization of composite materials. It achieved good effect in both near-field and far-field situations and was applied to the safety monitoring of aircraft. These methods use a nondestructive test signal as the reference to obtain information about the damage scattering wave. However, in practice, owing to environmental changes, probe coupling, and human error, consistent measurement conditions are difficult to obtain between the measured and baseline signals, possibly compromising the imaging accuracy. To prevent measurement problems, various methods for baseline-free damage imaging based on different principles have been

developed. Kannusamy et al. [5] and Poddar et al. [6] used the time-reversal method for baseline-free damage imaging to evaluate damage information in the excitation-reception path by analyzing the similarity between the input and reconstructed signals. However, other traveling waves (e.g., boundary echo waves) can interfere with the reverse signal, seriously undermining detection when applied to specimens with complex shapes. Ruzzene [7], Michaels et al. [8], and Yu et al. [9] extracted specified modes and damaged scattering waves through frequency-wavenumber domain filter (f-k filter) for damage imaging. As f-k filter requires the acquisition of complete wavefield data, the corresponding methods use scanning laser Doppler vibrometers to record the wavefield, but this setup is costly and only suitable for laboratory settings. On the other hand, piezoelectric transducers (PZTs) should be densely arranged to ensure wavefield measurement integrity [10], thus complicating detection.

Compressed sensing provides a basis for large-scale data compression. When a signal is sparse, compressed sensing allows to reconstruct a complete signal from few measurement points [11–13]. Therefore, data compression at the acquisition side has been leveraged for Lamb wave detection. Xu et al. [14] applied compressed sensing to sparse decomposition and reconstruction of Lamb waves, compensating for dispersion. Mesnil and Ruzzene [15] and Keshmiri Esfandabadi et al. [16] recovered complete wavefield data from sparsely measured signals and estimated the position of the scattering source. Chang et al. [17] applied compressed sensing to simplify dense sensor arrays while maintaining high tomographic imaging accuracy. Such compressed sensing-based methods streamline the data acquisition burden and can maintain a high detection accuracy under certain conditions, substantially improving their applicability.

Obtaining a priori information about structural integrity is difficult in large-scale structural health monitoring (SHM) system. Thus, this paper proposed a practical baseline-free damage imaging method using a PZT array to acquire wavefield data from a plate. Scattered waves are extracted from the wavefield in the frequency-wavenumber domain, and plate damage is then imaged based on the time of flight (TOF) of the scattering waves. This paper applied compressed sensing to simplify the placement of the PZT array considering the sparsity of Lamb waves in the frequency-wavenumber domain. A flowchart of the proposed method is shown in Figure 1.

The remainder of this paper is organized as follows. Section 2 briefly describes basic principles of probability imaging and compressed sensing. Section 3 details the reconstruction of wavefield data from Lamb waves by applying compressed sensing. Section 4 details feature wave extraction and probability imaging. Finally, we draw conclusions in Section 5.

2. Baseline-Free Imaging

2.1. Damage Probability Imaging.

This paper uses an algorithm for damage probability imaging based on ellipse location, as shown in Figure 2. Let T and R denote the

excitation device and sensor, respectively, and D denote damage. Detection is performed in the pitch-catch mode. The Lamb wave is generated by excitation device T to reach damage location D, and a scattering wave is generated at the damage location and acquired by sensor R. In this process, TOF t_d of the Lamb waves is given by

$$t_d = \frac{l_{TD} + l_{DR}}{c_g}, \tag{1}$$

where l_{TD} is the length of the path from T to D, l_{DR} is the length of the path from D to R, and c_g is the group velocity of the Lamb waves. Based on the estimated TOF and velocity c_g, the damage can be localized on ellipse e with foci T and R.

For arbitrary point $A(x, y)$ on the detected structure, the damage probability is positively correlated with its distance from ellipse e. A Gaussian function can define the damage probability distribution as

$$p(x, y) = \frac{1}{\sigma \sqrt{2\pi}} \exp\left(-\frac{\left(d_{AT} + d_{AR} - \hat{t}_d \cdot c_g\right)^2}{2\sigma^2}\right), \tag{2}$$

where σ is the standard deviation, d_{AT} and d_{AR} are the distances from point A to device T and sensor R, respectively, and $\hat{t}_d$ is the estimated TOF.

N independent T-R detection channels are calculated, and the obtained $p(x, y)$ is accumulated to determine the damage probability distribution field of the detected structure as follows:

$$DP(x, y) = \frac{1}{N} \sum_{i}^{N} p_i(x, y). \tag{3}$$

The most critical step is to obtain the TOF of the Lamb waves along the T-D-R path. During detection, the presence of several boundary echo waves and scattering waves hinders the direct extraction of defective scattering waves from the waveform acquired by sensor R. To address this problem, this paper uses a linear sensor array that includes an excitation device T and several sensors R_1-R_n, as shown in Figure 3. These elements are separated according to the features of the damage scattering wave in the wavenumber domain.

The Lamb waves received by the sensor array can be described by equation (4) as a superposition of traveling waves:

$$u(x, t) = \sum_{i} A_i \exp[j(k_i x - \omega_i t)], \tag{4}$$

where A_i is the amplitude of the traveling wave. In the linear array shown in Figure 3, the rightward direction is positive. Direct wave P1 from actuator T is a rightward traveling wave with wavenumber $k > 0$, whereas scattering wave P2 from a damage is a leftward traveling wave with $k < 0$. They can be separated by their features in the wavenumber domain.

The data from sensors R_1-R_n are sequentially arranged to form matrix $R(x, t)$, to which the two-dimensional fast Fourier transform is applied to obtain a representation in the frequency-wavenumber domain as follows:
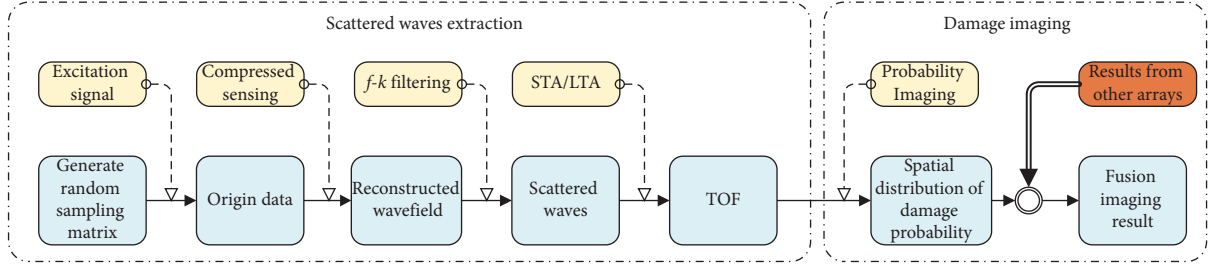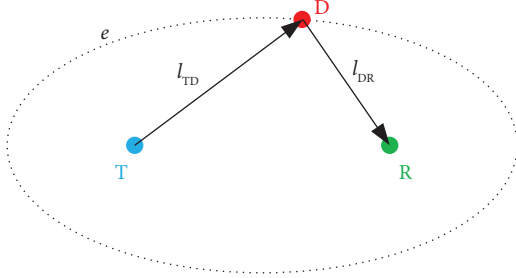
FIGURE 1: Flowchart of the proposed method.

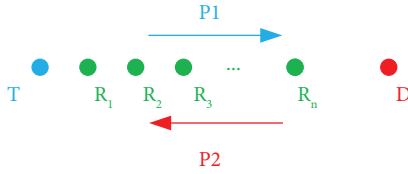FIGURE 2: Principle of ellipse location.

FIGURE 3: Linear sensor array.

$$G(k_m, \omega_n) = \sum_{p=0}^{N_t-1} \sum_{q=0}^{N_x-1} R(x_p, t_q) \exp\left[-2\pi j\left(k_m x_p + f_n t_q\right)\right], \quad (5)$$

where $G(k, \omega)$ is the frequency-wavenumber spectrum and N_t and N_x are the sampling points in the time and distance domains, respectively. The wavenumber of damage scattering wave P2 is negative when the damage is located along the sensor array. In the frequency-wavenumber spectrum, f-k filter is applied to extract the components with negative wavenumbers, and then the two-dimensional inverse Fourier transform is applied to obtain the wavefield of damage scattering wave P2 in the time-distance domain.

2.2. Compressed Sensing.
The sensor array depicted in Figure 3 is sampled at equal intervals, and the resolution of the Fourier spectrum is F_s/N_s, where F_s is the sampling frequency. In the distance domain, F_s is the reciprocal of sensor spacing δ and N_s is the number of sampling points. To recover the analog signal without distortion, the sampling frequency should be higher than the Nyquist frequency. In practice, to obtain more details of the waveform signal, the sampling frequency is usually set to 3–15 times the Nyquist frequency [18]. As the sampling frequency increases, more sampling points are required to obtain a more accurate Fourier spectrum, substantially

increasing the computational burden for detection. To prevent this problem, this paper uses uneven sampling at a frequency much lower than the Nyquist frequency and reconstructs the subsampled data using compressed sensing.

As data in the time domain can be read continuously and automatically by a digital acquisition system, subsampling is not performed in this domain. Let the Nyquist sampling signal have m sampling points in the distance domain and n sampling points in the time domain.

$$\mathbf{Y} = \mathbf{X}_{\Phi}^{s\,T}, \quad (6)$$

where $\mathbf{X} \in \mathbb{R}^{n \times m}$ is the signal sampled at the Nyquist frequency and $\Phi_s \in \mathbb{R}^{q \times m}$ is the observation matrix in the distance domain. Subsampling method implements uneven interval random sampling on the complete Nyquist sampling matrix, in which q locations in m equally spaced arrays are randomly selected to place sensors for measurement. The observation matrix Φ_s corresponding to this subsampling approach is a random Bernoulli matrix, whose construction is described in Algorithm 1.

Sampled data $\mathbf{Y} \in \mathbb{R}^{n \times q}$ are obtained from equation (6). In compressed sensing, a necessary condition for the exact recovery of $\mathbf{X}$ from subsampled data $\mathbf{Y}$ is that $\mathbf{X}$ is sparse in a transform domain [10].

$$\mathbf{X} = \Psi_t^{-1} \mathbf{C} \Psi_s^{-1}, \quad (7)$$

where Ψ_t and Ψ_s are Fourier transform matrices of sizes $n \times n$ and $m \times m$, respectively, $\mathbf{C} \in \mathbb{C}^{n \times m}$ is the sparse coefficient matrix, and subsampling data $\mathbf{Y}$ are described by

$$\mathbf{Y} = \Psi_t^{-1} \mathbf{C}_{\mathbf{H}}^{s\,T},$$
$$\mathbf{H}_s = \Phi_s \Psi_s. \quad (8)$$

The reconstruction of $\mathbf{X}$ can be decomposed to process each row of $\mathbf{X}$, establishing an underdetermined problem. Considering the presence of noise effects in the model, optimization by $l1$ minimization is implemented using basis pursuit denoising (BPDN) [19]. The rows of matrices $\mathbf{Y}$ and $\mathbf{C}$ have the form shown in the following equation:

$$\mathbf{Y} = \left(y_1^T, y_2^T, \ldots, y_n^T\right)^T,$$
$$\mathbf{C} = \left(c_1^T, c_2^T, \ldots, c_n^T\right)^T. \quad (9)$$

For reconstruction of the i-th row, the optimization objective is given by

```
Initialize:
    int a: the length of original data
    int b: the number of sub-Nyquist sampling points.
    mat Φ: sub-Nyquist sampling matrix.
Ensure: a > b
(1)  Φ ⟵ zeros (b, a) % initialize Φ as a b × a zero matrix.
(2)  array pset ⟵ randperm (a, b) % randperm(a, b) returns an array containing b unique integers selected randomly from 1 to a.
(3)  array pset ⟵ sort (pset) % sort the elements of pset.
(4)  for (row = 1 to b) do
(5)      col ⟵ pset [i]
(6)      Φ [row, col] ⟵ 1
(7)  end for
(8)  return Φ
```

ALGORITHM 1: Construction method of sub-Nyquist sampling matrix.

$$\arg\min_{c} \|c\|_1 \text{ subject to} \|y_i - \mathbf{A}_i\|_2^2 \le \sigma \mathbf{A} = \mathbf{\Psi}_t^{-1} \mathbf{C}_H^{sT}, \quad (10)$$

where $\mathbf{A}_i$ is the i-th row of matrix $\mathbf{A}$ and σ is the noise characteristic parameter, whose value depends on the estimated noise level. This paper uses the $l1$ norm as a constraint to solve the NP-hard problem in $l0$ norm optimization. When noise is present, element 0 in the sparse vector is not strictly equal to 0. Therefore, the optimal solution cannot be obtained by applying the $l0$ norm constraint to optimization. Instead, an optimal convex approximation of the original problem using the $l1$ norm can be obtained for an approximate sparse solution of the vector [20, 21].

In subsampling for the distance domain, let the length of observed data be q and that of the Nyquist sampled data be m. The data compression ratio is defined as

$$CR = \left(1 - \frac{q}{m}\right) \times 100\%. \quad (11)$$

According to Candes and Tao [22], to recover the characteristic information of Nyquist sampled signals without distortion, the observation matrix must satisfy the restricted isometry property (RIP). Specifically, for signal y with sparsity K and an arbitrary constant δ_k, the following condition must be satisfied:

$$(1 + \delta_k)\|y\|_2^2 \le \|\Phi y\|_2^2 \le (1 + \delta_k)\|y\|_2^2. \quad (12)$$

It is difficult to verify whether equation (12) is valid experimentally. When the observation matrix is random, for a subsampling of data in a particular domain, the restricted isometry property has the following sufficient conditions [10]:

$$N_{\text{sub}} \ge K \log\left(\frac{N_{\text{nyq}}}{K}\right), \quad (13)$$

where N_{nyq} is the number of Nyquist sampling points and N_{sub} is the number of subsampling points. For this example of two-dimensional data, equation (13) has the following expansion:

$$q \ge \frac{K}{n} \log\left(\frac{mn}{K}\right). \quad (14)$$

When the RIP satisfied, q exists at a lower bound; that is, there is an upper bound on the data compression ratio.

3. Extraction of Scattering Waves

3.1. Experimental Setup. As the experimental specimen, this paper selected a $1000 \times 1000 \times 3.5$ mm aluminum plate with longitudinal wave velocity $c_L = 6115$ m/s and transverse wave velocity $c_S = 3123$ m/s. Two circular hole-shaped defects with a diameter of 20 mm and 10 mm were created in the middle of the plate. The experimental setup mainly consisted of a data acquisition industrial personal computer (NI™ PXIe-1082, National Instruments, USA), power amplifier (AG 1020, T&C, USA), actuator, and sensor, as shown in Figure 4. A waveform generator (NI™ PXIe-5423, National Instruments, USA) and high-speed oscilloscope (NI™ PXIe-5105, National Instruments, USA) were installed in the computer. The actuator was a Fujicera 1045S probe, and the receiver was a PZT (PZT-5, Coremorrow, CHN) with 4 mm diameter Plate and PZT are coupled using gel coupler. The semianalytical finite element (SAFE) method is used to calculate the dispersion curves of plate structures. Figure 5 shows the group velocity dispersion curve of the aluminum plate with a thickness of 3.5 mm. It can be seen that the A0 mode has stable group velocity variation above 70 kHz. To simplify the number of sensors, low-frequency excitation should be used to obtain longer wavelength Lamb waves. Considering the operating frequency of the sensor and the propagation ability of Lamb wave, a seven-cycle sinusoidal modulated waveform with center frequency of 100 kHz was used as the excitation signal. Measurements were made in the pitch-catch mode. The reference line of each PZT position in the array is predrawn on the plate, and the array was implemented by moving the PZT to multiple positions. The sampling rate was 2 MSa/s, and the excitation signal was used as the reference signal to synchronize the acquired datasets.

3.2. Subsampling. To design appropriate subsampling arrays, the frequency-wavenumber spectrum of Lamb wave wavefield in the plate is analyzed in advance. A dense array is
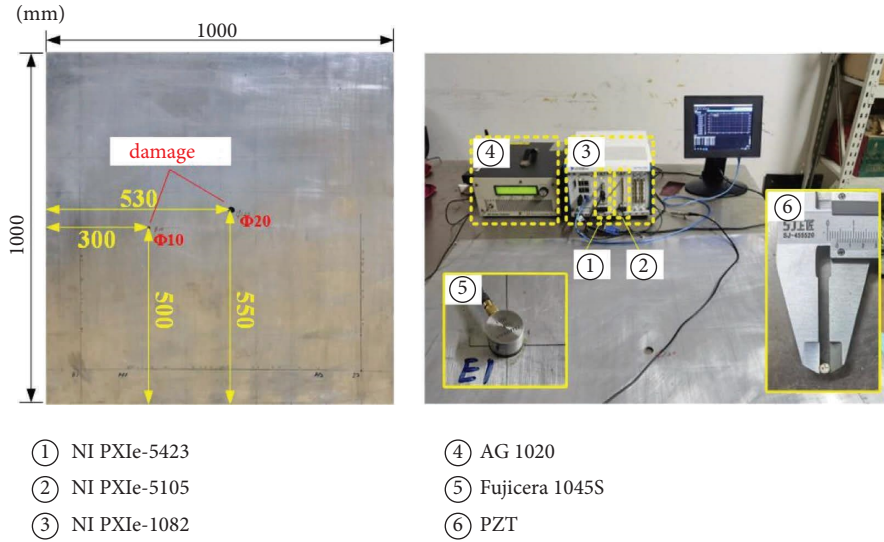
FIGURE 4: Experiment setup.

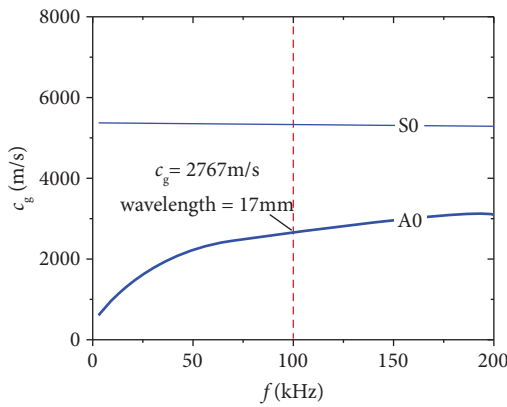|			
① NI PXIe-5423		④ AG 1020	
② NI PXIe-5105		⑤ Fujicera 1045S	
③ NI PXIe-1082		⑥ PZT	

FIGURE 5: Group velocity curve for aluminum plate with thickness of 3.5 mm.
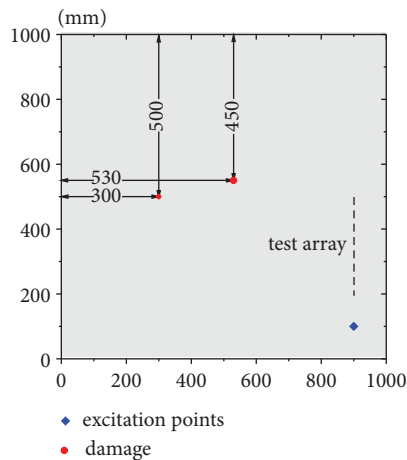

FIGURE 6: Dense array for wavefield test.

placed on one side of the plate, as shown in Figure 6. The sensor interval is 4 mm with 76 acquisition points and the total length of the array is 300 mm. Figure 7(a) shows the partial measurement point signals when array was subjected to Nyquist sampling, which can be used to analyze the wavefield features of Lamb waves. Several wave packets that are easier to distinguish are, in order of appearance, the direct wave, the near-end echo, and the far-end echo, while the other wave packets have low signal to noise ratio (SNR). It is difficult to extract the damage scattering waves directly from the signal because there is no baseline signal for reference.

To determine the minimum observation length that satisfies the RIP condition, the signal sparsity must be calculated according to equation (14). This paper applied the two-dimensional Fourier transform (2-D FFT) to the data from the 76 sampling points of array to obtain the frequency-wavenumber spectrum, as shown in Figure 7(b). In the spectrum, regions with larger amplitudes are clustered near the dispersion curve of A0 mode. As shown in Figure 8, most of the data are distributed around 0. The frequency-wavenumber spectrum is approximately sparse when regions with small amplitudes are considered as noise. This noise is discarded for reconstruction. When a value below 0.8% of the maximum amplitude was selected as noise, sparsity K of the frequency-wavenumber spectrum was 3690. In equation (14), $m = 76$, $n = 2000$, and the minimum number of sampling points for subsampling was 7. To recover feature information of the original wavefield without distortion, 10 sampling points were selected to reconstruct the original wavefield, representing a compression ratio of 86.7%.
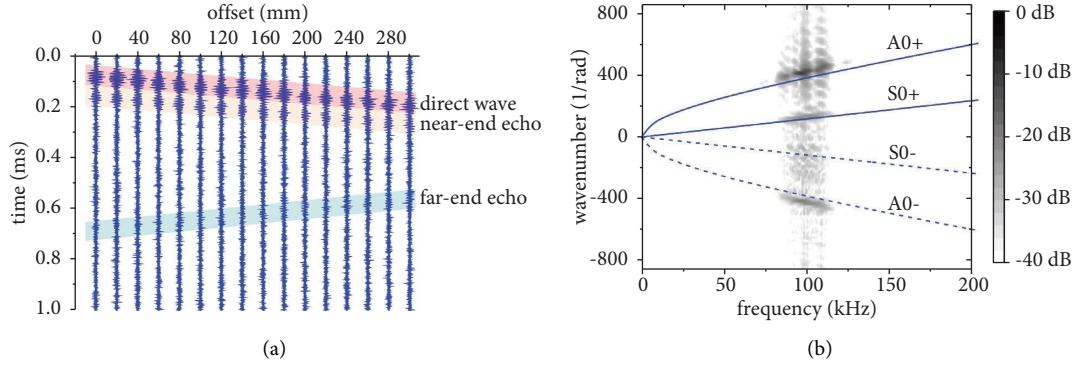
(a)

(b)

FIGURE 7: The (a) wavefield recording of the test array and (b) its frequency-wavenumber spectrum; the three largest amplitude wave packets of each signal are the direct wave, the near-end echo, and the far-end echo.
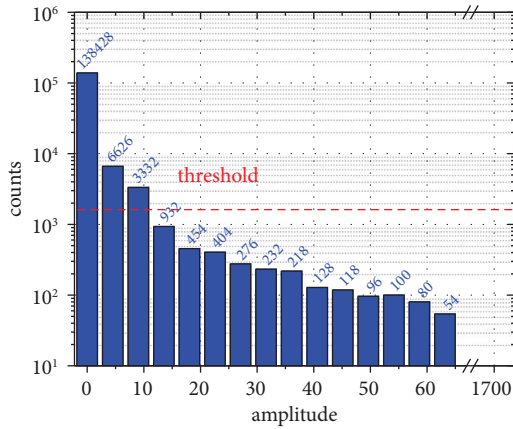

FIGURE 8: The amplitude distribution of the frequency-wavenumber spectrum of the test array, when taking 0.8% of the maximum value as the threshold value.
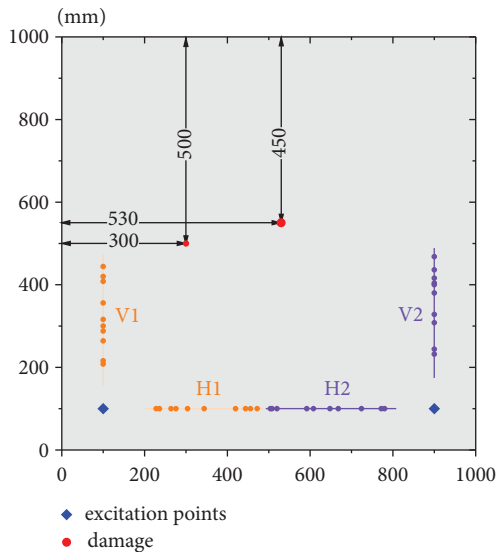

FIGURE 9: Arrangement of subsampling arrays.

Based on the results of the above analysis, four arrays of sensors were set up, as illustrated in Figure 9, which include two horizontal direction arrays denoted as H1 and H2 and

two vertical direction arrays denoted as V1 and V2. The minimum sampling interval, δ, was set to 4 mm, and the sensor array measurement length was 300 mm. Figure 10(a) shows the frequency-wavenumber spectrum reconstructed for 10 sampling points. To verify the contribution of compressed sensing, the reconstruction results (Figure 10(b)) were compared with those obtained according to the Nyquist sampling theorem for the same number of sampling points. The characteristics of the frequency-wavenumber spectrum show that reconstruction using compressed sensing agrees with the original wavefield, with larger amplitudes around mode A0. In contrast, the frequency-wavenumber spectrum obtained according to the strict requirement of the Nyquist sampling theorem hardly shows the dispersion of each mode owing to the small number of sampling points. The root-mean-square error (RMSE) was used to quantify the error between the original frequency-wavenumber spectrum and the reconstruction result:

$$\text{RMSE} = \sqrt{\frac{1}{mn} \sum \left[C(\omega, k) - G(\omega, k) \right]^2}, \quad (15)$$

where m and n are the data lengths in the distance and time domains of the Nyquist sampling data, respectively, $G(\omega, k)$ denotes the original frequency-wavenumber spectrum, and $C(\omega, k)$ denotes the reconstructed frequency-wavenumber spectrum. An RMSE of 514 in Figure 10(a) is obtained from reconstruction using compressed sensing, while an RMSE of 1519 is obtained for Figure 10(b). Overall, the wavefield features of Lamb waves can be reconstructed more accurately using compressed sensing than when considering Nyquist sampling at the same data compression ratio while substantially reducing the workload of data acquisition.

4. Damage Imaging

4.1. Scattering Wave Extraction. Consider array V2 as an example to illustrate scattering wave extraction. Under excitation perpendicular to the plate plane, mode A0 is dominant in Lamb wave propagation. According to the propagation direction of the wave packet, each mode is
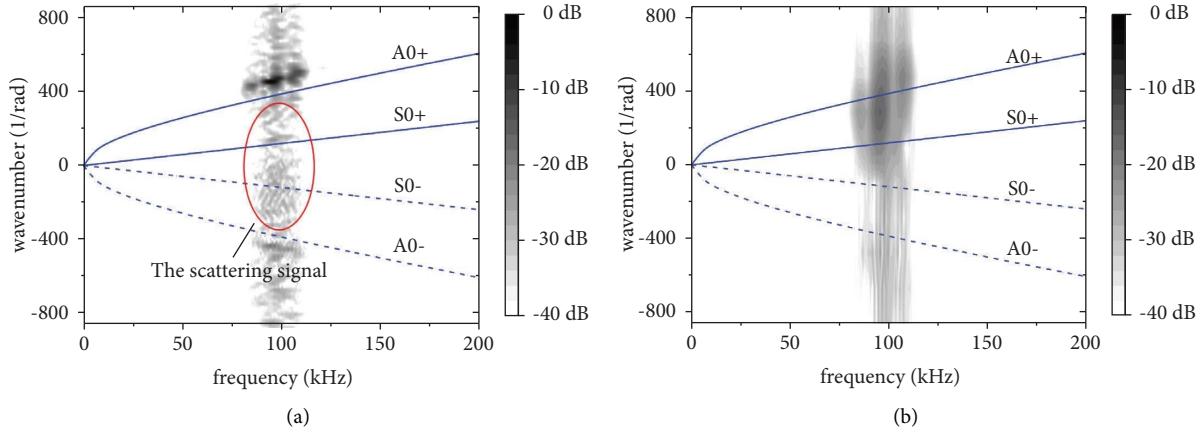
FIGURE 10: Comparison of the frequency-wavenumber spectrum reconstructed by applying both (a) compressed sensing and (b) Nyquist sampling followed by direct transformation, both using 10 sampling points.
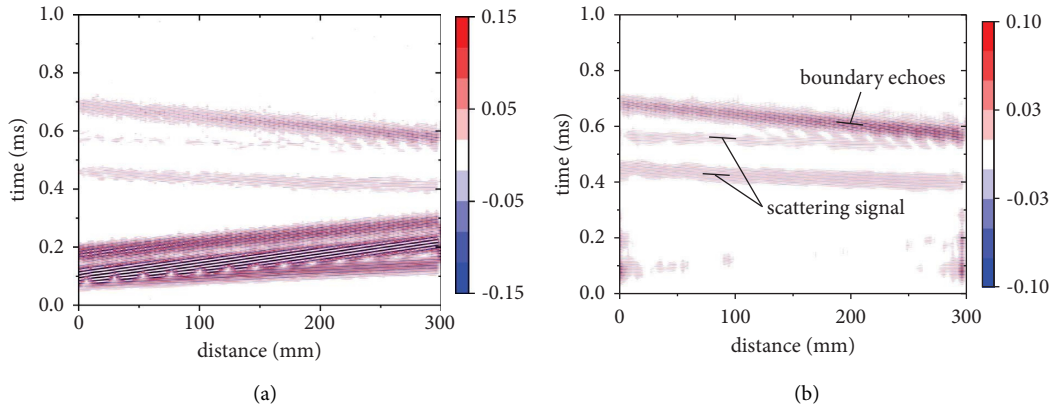

FIGURE 11: The (a) original wavefield and (b) wavefield with negative wavenumber acquired from the V2 array, mainly composed of damage scattering waves and far-end echoes.

divided into two states with positive (A0+, S0+) and negative (A0−, S0−) wavenumbers. The major components of A0+ are the direct wave and near-end echoes, and those of A0− are the far-end echoes. The scattered wave observed by the sensor array does not satisfy the Lamb wave dispersion relationship because the damage does not lay along the sensor array line, resulting in a wavelength larger than the actual value. Therefore, in the frequency-wavenumber spectrum (Figure 10(a)), the scattering wave components are distributed between modes with wavenumbers A0 and A0+, with no obvious dominant mode.

Equation (3) describes the probability imaging algorithm that requires extraction of damage scattering waves. Probability imaging is different from the model depicted in Figure 3, where the wavefield with a positive wavenumber contains the damage scattering wave because the damage is not colinear with the sensor array. By analyzing the frequency-wavenumber spectrum, the amplitude of the Lamb wave propagating along the positive direction is much larger than that along the negative direction. Lamb waves propagating along the positive direction have more components that mainly contain direct waves, near-end echoes, and damage scattering waves. For clarity, all the components in

the frequency-wavenumber spectrum with wavenumbers less than 0 are separated, and the inverse Fourier transform is applied to reconstruct the wavefield. As the reconstructed coefficient matrix is not conjugate symmetric, the real part of the inverse transform is taken as the reconstructed wavefield for analysis, as shown in Figure 11. The two groups of traveling waves can be clearly distinguished in the wavefield. The relative positions of the sensor arrays can be used to determine the two sets of traveling waves as the distal boundary echo and damage scattering wave. Given that the boundary cross section is perpendicular to the direct wave propagation direction, energy scattering in other directions at the boundary is lower, and the amplitude of the detected boundary echo is larger. On the other hand, the energy of the damage scattering wave is smaller. By projecting the traveling direction of the damage scattering wave onto the sensor array line, after frequency-wavenumber domain filtering, only the traveling wave whose projection is opposite to the propagation direction of the direct wave is retained.

The short-time average to long-time average (STA/LTA) algorithm is commonly used in seismic monitoring to extract the first arrival instant of seismic waves [23]. This paper uses the STA/LTA algorithm to calculate the TOF of

the damage scattering waves. Given a long-time window of length N_L sliding within the time series, a short-time window of length N_S is considered to slide within the long-time window. The corresponding LTA and STA are calculated using a characteristic function. The LTA characterizes the variation of background noise, and the STA characterizes the variation of the Lamb wave. When the signal arrives, the STA changes faster than the LTA, and the STA/LTA value increases rapidly. This process is described as follows:

$$\text{STA}(i) = \frac{1}{N_S} \sum_{i=1}^{N_S} \text{CF}(i),$$

$$\text{LTA}(i) = \frac{1}{N_L} \sum_{i=1}^{N_L} \text{CF}(i), \tag{16}$$

$$\kappa(i) = \frac{\text{STA}(i)}{\text{LTA}(i)},$$

where CF(i) is the characteristic function, which should be sensitive to the signal arrival. Under short-time excitation and mild dispersion, the collected Lamb wave is transient. The energy of the signal changes substantially before and after the Lamb wave arrival. Thus, this paper uses CF(i) = $x(i)$ [2] as the characteristic function.

Data $r(i)$ of the 10th sampling point in the wavefield reconstructed by array V2 were selected for analysis. The distance between this sampling point and the excitation device T was 140 mm. Values $\kappa(i)$ of data series $r(i)$ were calculated. For parameter selection, short-time window length N_S should be 3–5 times the signal period and long-time window length N_L should be 4–10 times N_S to balance the sensitivity and false pickup rate of detection [24]. This paper sets $N_S = 50$ and $N_L = 500$, obtaining the results shown in Figure 12. The blue line denotes the signal after f-k filtering, which retains only the components with negative wavenumber. The peak of κ can establish the instant of arrival of the corresponding wave packet. We recorded the peak points of the first 4 amplitude values in the $\kappa(i)$ series and denoted them as P1, P2, P3, and P4 in descending order of amplitude; the results are shown in Figure 13.

We analysed the effective detection area of the plate when using the array to extract the damage scattering waves. Figure 14(a) depicts the relative positions of the array and the damage. The relationship between the probability of being able to extract a damage scattering wave and θ is obtained by moving the array position, as shown in Figure 14(b). The maximum allowable error is set to 0.1 ms for statistics. The probability of extraction using the STA/LTA method gradually decreases as θ increases. For any point A on the plate, when damage is present at that location, the following equation can be used to evaluate the degree of contribution of each array to the damage extraction and thus characterize the damage sensitivity of each region.

$$S = \beta \cdot \sum_{i}^{m} \lambda_i P_e (\cos \theta_i), \tag{17}$$

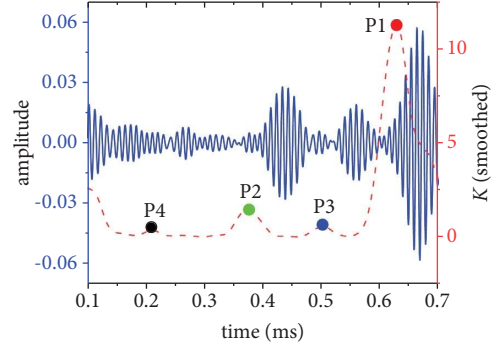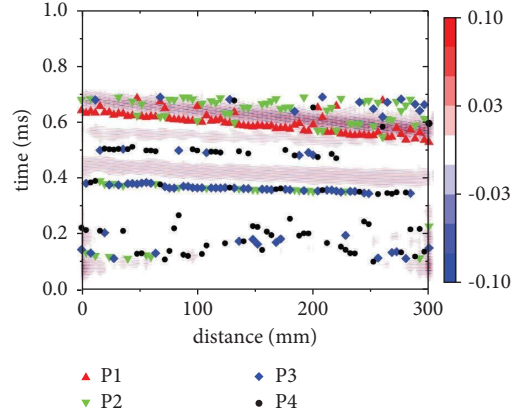
FIGURE 12: Extract TOF of Lamb wave using STA/LTA.

FIGURE 13: Recognition results of TOF of wave reflected from defects in the wavefield.

λ_i is the contribution parameter of sensor R_i and its value depends on the relative position of point A to sensor R_i. When $|TF| > |TR_i|$, $\lambda_i = 1$; otherwise, $\lambda_i = 0$. The reason for this design is that when $|TF| > |TR_i|$, the wavenumber of the scattered wave is negative and can be extracted by the f-k filter. Point B is the intersection of the array line and the boundary. In the detection, the boundary echo emitted from point B is the main interference source, and the scattered waves emitted from the damage near the location of point B will be drowned out. The interference condition is supplemented by adding the value of β. When $|AB| > \delta$, $\beta = 1$; otherwise $\beta = 0$. δ depends on the Lamb wave wavelength and the number of periods, and $\delta = 0.15$ m is taken in this case. The calculated damage sensitivity of each region in the plate is shown in Figure 14(c). The results in the figure are superimposed on the results of the four sensor arrays. It can be seen that with such a sensor arrangement, the sensitivity is highest in the middle position of the plate, while the sensitivity is poorer on both sides close to the array and at the lower end position. When designing the scheme, the key monitoring locations should be arranged far from the array to improve the monitoring success rate.

4.2. Probability Imaging. We used equations (2) and (3) to calculate the damage probability distribution fields of each array, obtaining the results shown in Figure 15 for standard
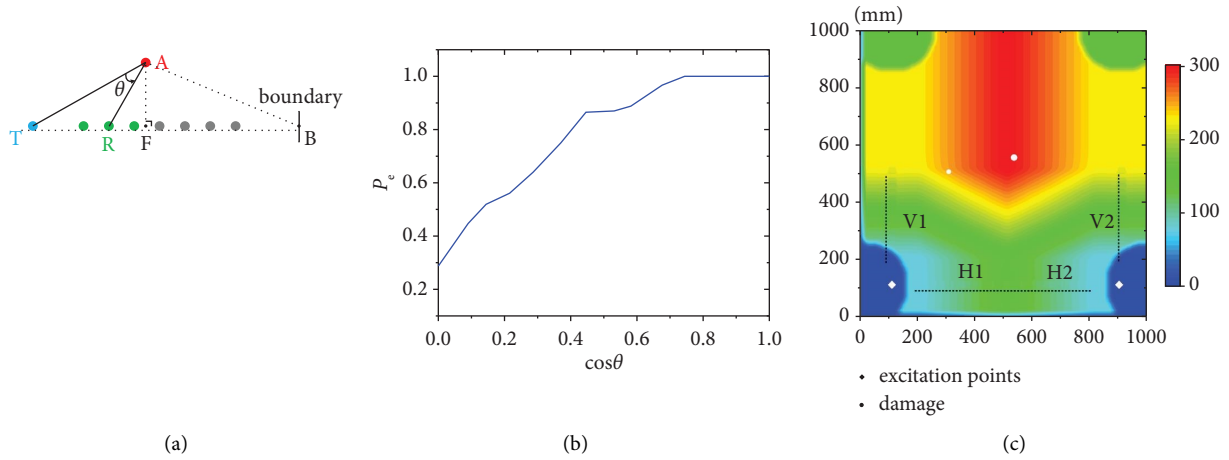
(a) (b) (c)

FIGURE 14: (a) Schematic of sensor array. (b) P_e. (c) Damage sensitivity at each location in the plate.
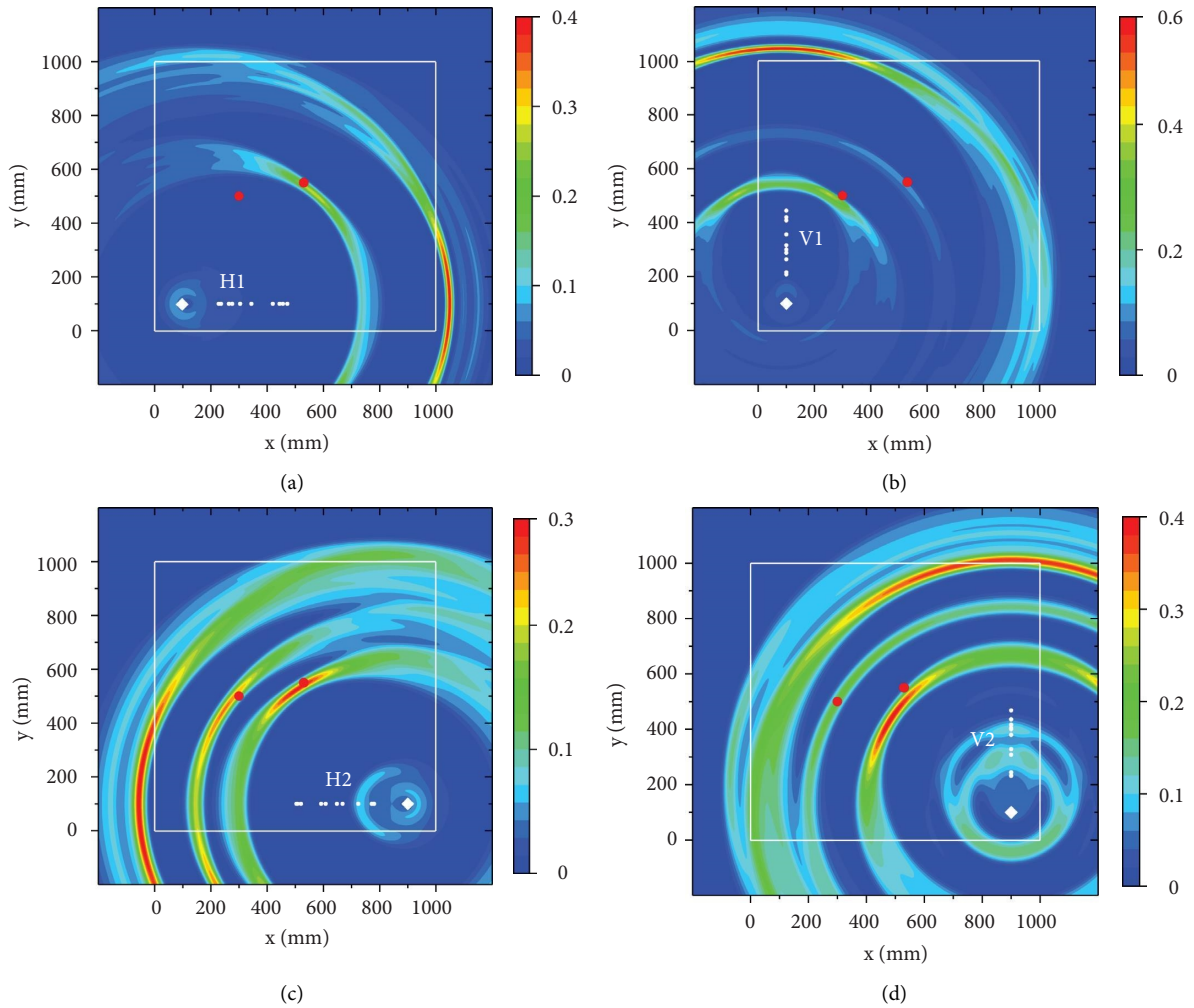

(a) (b)

(c) (d)

FIGURE 15: Damage probability imaging results calculated from (a) H1, (b) V1, (c) H2, and (d) V2.

deviation σ set to 0.025. Mode A0 is dominant for the plate Lamb waves with group velocity $c_g = 2767$ m/s at 100 kHz from the dispersion curve. The white rectangle in Figure 15 represents the plate boundary, and the red dot represents the

damage location. Each group of sensor arrays can roughly locate the damage but lacks sufficient imaging accuracy. In addition, the magnitude of the boundary area is much higher than that of the damage in the imaging results. As the
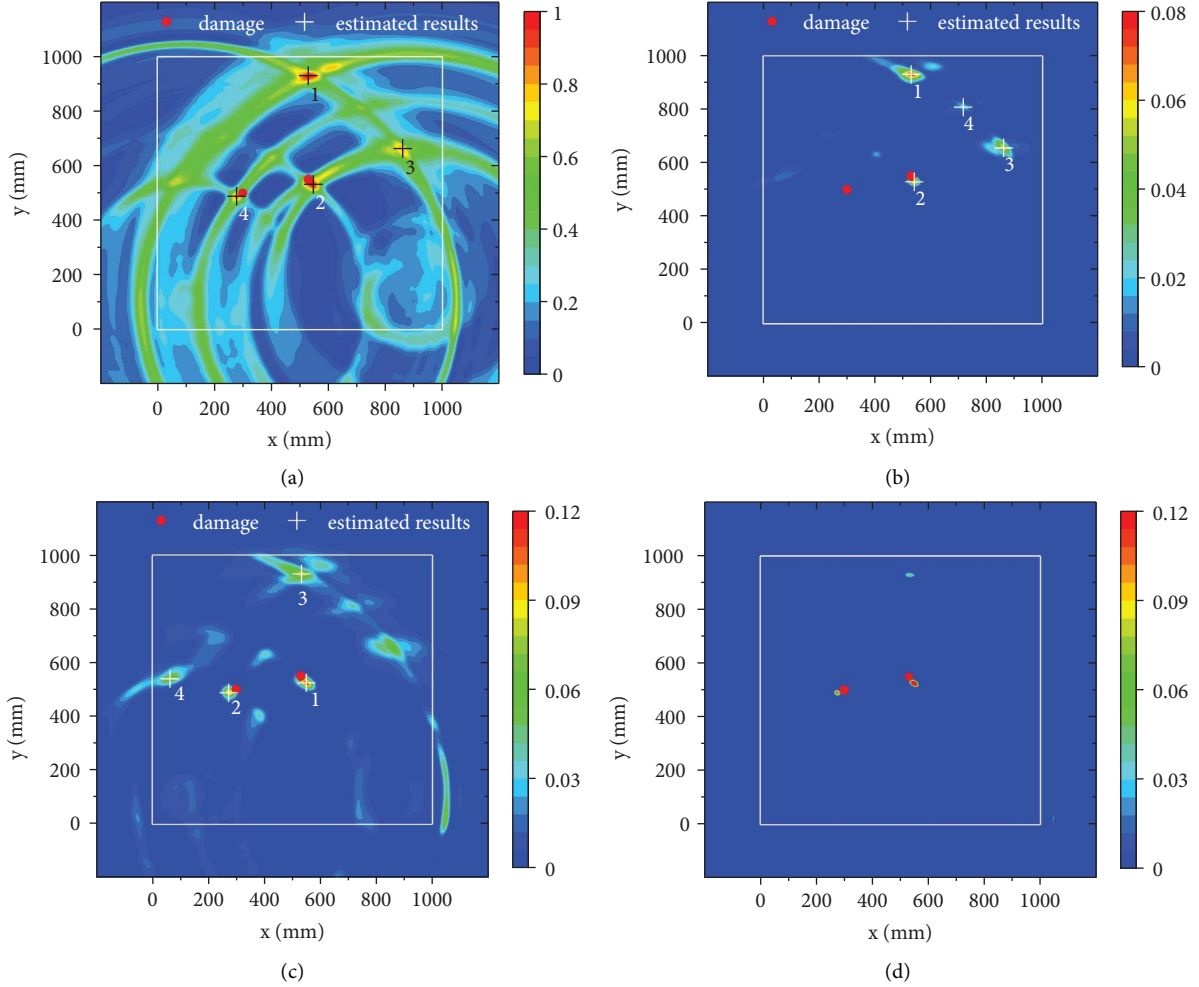
(a)

(b)

(c)

(d)

FIGURE 16: Damage probability distribution obtained by (a) direct accumulation, (b) cumulative multiplication, and (c) combining amplitude addition and multiplication. (d) Result (c) after −3 dB threshold processing ("+" is the local maximum of the damage probability, the order of magnitude of which has been marked by the numbers 1–4).

actuators are colinear with the sensor array, the angle between the tangents of each ellipse at the damage location is small. Thus, imaging provides a dense cluster of ellipses near the damage location when multiple results are accumulated, leading to an artifact at a symmetric location below the sensor array line.

To improve imaging quality, this paper used the imaging results from multiple arrays. The results of multiple images are typically fused by applying addition or multiplication. Figure 16(a) shows the results obtained by directly accumulating the damage probability distributions of all the arrays. Compared with imaging considering a single array, accumulation suppressed artifacts. However, the fusion results retain too much of the single array results, such as the boundary and nearby regions. This cannot highlight the results at the location of the damages, easily leading to incorrect damage localization. As each array reflects a different boundary region, using cumulative multiplication can eliminate the effect of the plate boundary. Nevertheless, Due to the weak imaging capability of the H1 array for left-sided damage, as shown in Figure 16(a), imaging from every array

has an excessive influence on the overall fusion. It was almost impossible to estimate the location of the left-sided damage from the fusion result using cumulative multiplication, as shown in Figure 16(b).

Based on the sensor array shown in Figure 6, this paper combined amplitude addition and multiplication for imaging fusion. Combine horizontal array and vertical array to form 2 array pairs. For each array pair, the results of the horizontal and vertical arrays were first processed using Hadamard products, and the results were then summed to obtain the final fusion results. The fusion process is described as

$$P(x, y) = p_{H1}(x, y) \cdot p_{V2}(x, y) + p_{H2}(x, y) \cdot p_{V1}(x, y). \quad (18)$$

This type of fusion has two advantages. First, there is a low correlation between the boundary imaging results of the horizontal and vertical arrays, and multiplication eliminates the influence of the plate boundary. Owing to the different array orientations, the imaging results of the dense ellipse clusters at the damage location cross with each other, and multiplication allows to locate the damage more accurately.

Second, the summation of the products prevents a particular array with unsuitable damage imaging from having an excessive effect on the overall results. By combining amplitude addition and multiplication, the imaging results mostly suppress plate boundaries. The two locations with the highest damage probability were consistent with the real damage locations, as shown in Figure 16(c). The accuracy of damage imaging improves substantially. After the -3 dB threshold processing (Figure 16(d)), the imaging results can show the location of the damage more clearly, and the effect of artifacts is reduced to some extent.

It is also important to note that even though the number of sensors was reduced using the compressed sensing method, 40 sampling points were still left. Compared to RAPID, MUSIC, and time-reversal-based imaging methods, more sensors need to be arranged. This is the price of keeping the imaging accuracy based on the baseline-free condition. The imaging method in this paper is based on the recovered complete wavefield, which is superior to the excitation-reception path scan-based method in terms of imaging accuracy [2, 3, 5, 25]. According to the characteristics of compressive sensing and ellipsoidal imaging, increasing the number of sensors can steadily improve the expectation accuracy and does not require too much consideration of the impact of sensor placement. This is one of the advantages of the proposed imaging method in this paper.

5. Conclusions

This paper proposed a method for baseline-free damage imaging based on Lamb waves and compressed sensing. The damage scattering waves in the wavefield are obtained by f-k filtering, and damage probability imaging is performed based on the TOF of the scattering waves. Results of imaging experiments on a plate with a circular hole damage validate the effectiveness of the proposed method.

The main contributions of this study are summarized as follows:

(1) Two-dimensional filters are designed according to the features of damage echoes in the frequency-wavenumber domain. The reflected waves at the damage are obtained by separating the components with negative wave numbers in the original wavefield. without requiring data from nondestructive tests as a baseline.

(2) Frequency-wavenumber domain filtering requires the acquisition of dense time-distance domain wavefield data using compressed sensing to improve applicability. Under the conditions described in this study, the wavefield can be recovered by selecting only 10 sampling points per linear array, representing a data compression ratio of 86.7% compared with Nyquist sampling.

(3) Applying the STA/LTA algorithm to implement automatic extraction of the damage scattering wave TOF, the arrival time of multiple feature waves can

be extracted. Thus, the proposed method can perform multiple-damage imaging in principle.

(4) Two orthogonally oriented sensor arrays were laid out, and the imaging results were fused by combining amplitude addition and multiplication. Hence, the influence of nondamaged regions on the imaging results is mostly suppressed, improving the imaging quality.

Overall, the proposed method achieves accurate baseline-free imaging of damage in plates and may be applied for monitoring specimens with plate shape. Nevertheless, the proposed method has some application limitations. First, the case in this study uses only mode A0 for imaging because this mode is dominant under low-frequency asymmetric excitation. For small damages in a plate, Lamb waves at high frequencies must be used and analyzed. However, there are more modes with different group velocities in high frequencies. Thus, the design of the frequency-wavenumber filter should be extended to separate the modes. Second, the sensitivity to damage varies for imaging at each plate location. For damage close to the actuator, data of damage scattering waves in the wavefield are scarce, possibly leading to poor imaging results. In addition, the feature waves extracted with the f-k filter still contain many scattering waves at nondamaged locations due to the absence of a baseline reference, which is the largest error source in the proposed method and leads to the inclusion of some artifacts in the imaging results. In future work, we will explore improvements to overcome this and other limitations of the proposed method.

Data Availability

The data used to support the findings of this study are included within the article.

Conflicts of Interest

The authors declare that they have no conflicts of interest regarding the publication of this paper.

Acknowledgments

References

[1] P. Kudela, M. Radzienski, and W. Ostachowicz, "Structural health monitoring system based on a concept of lamb wave focusing by the piezoelectric array," *Mechanical Systems and Signal Processing*, vol. 108, pp. 21–32, 2018.

[2] H. Huo, J. He, and X. Guan, "A bayesian fusion method for composite damage identification using lamb wave," *Structural Health Monitoring*, 2020.

[3] Y. Liu, X. Hong, and B. Zhang, "A novel velocity anisotropy probability imaging method using ultrasonic guided waves for composite plates," *Measurement*, vol. 166, Article ID 108087, 2020.

[4] S. Yuan, Y. Zhong, and Q. Lei, "Two-dimensional near-field multiple signal classification algorithm-based impact localization," *Journal of Intelligent Material Systems and Structures*, vol. 26, no. 4, pp. 703-704, 2015.

[5] M. Kannusamy, S. Kapuria, and S. Sasmal, "Accurate baseline-free damage localization in plates using refined Lamb wave time-reversal method," *Smart Materials and Structures*, vol. 29, no. 5, Article ID 055044, 2020.

[6] B. Poddar, A. Kumar, M. Mitra, and P. M. Mujumdar, "Time reversibility of a lamb wave for damage detection in a metallic plate," *Smart Materials and Structures*, vol. 20, no. 2, pp. 025001–025010, 2011.

[7] M. Ruzzene, "Frequency–wavenumber domain filtering for improved damage visualization," *Smart Materials and Structures*, vol. 16, no. 6, pp. 2116–2129, 2007.

[8] T. E. Michaels, J. E. Michaels, and M. Ruzzene, "Frequency-wavenumber domain analysis of guided wavefields," *Ultrasonics*, 2011.

[9] L. Yu, C. A. C. Leckey, and Z. Tian, "Study on crack scattering in aluminum plates with Lamb wave frequency–wavenumber analysis," *Smart Materials and Structures*, vol. 22, no. 6, Article ID 065019, 2013.

[10] L. Qiu, B. Liu, S. Yuan, and Z. Su, "Impact imaging of aircraft composite structure based on a model-independent spatial-wavenumber filter," *Ultrasonics*, vol. 64, pp. 10–24, 2016.

[11] D. L. Donoho, "Compressed sensing," *IEEE Transactions on Information Theory*, vol. 52, no. 4, pp. 1289–1306, 2006.

[12] D. J. Holland, D. M. Malioutov, A. Blake, A. Sederman, and L. Gladden, "Reducing data acquisition times in phase-encoded velocity imaging using compressed sensing," *Journal of Magnetic Resonance*, vol. 203, no. 2, pp. 236–246, 2010.

[13] Z. Wang, S. Huang, G. Shen, S. Wang, and W. Zhao, "High resolution tomography of pipeline using multi-helical lamb wave based on compressed sensing," *Construction and Building Materials*, vol. 317, Article ID 125628, 2022.

[14] C. b. Xu, Z. b. Yang, X. f. Chen, S. Tian, and Y. Xie, "A guided wave dispersion compensation method based on compressed sensing," *Mechanical Systems and Signal Processing*, vol. 103, pp. 89–104, 2018.

[15] O. Mesnil and M. Ruzzene, "Sparse wavefield reconstruction and source detection using compressed sensing," *Ultrasonics*, vol. 67, pp. 94–104, 2016.

[16] Y. Keshmiri Esfandabadi, L. De Marchi, N. Testoni, A. Marzani, and G. Masetti, "Full wavefield analysis and damage imaging through compressive sensing in Lamb wave inspections," *IEEE Transactions on Ultrasonics, Ferroelectrics, and Frequency Control*, vol. 65, no. 2, pp. 269–280, 2018.

[17] M. Chang, S. Yuan, and F. Guo, "Corrosion monitoring using a new compressed sensing-based tomographic method," *Ultrasonics*, vol. 101, Article ID 105988, 2020.

[18] V. Serey, N. Quaegebeur, M. Renier, P. Micheau, P. Masson, and M. Castaings, "Selective generation of ultrasonic guided waves for damage detection in rectangular bars," *Structural Health Monitoring*, vol. 20, no. 3, pp. 1156–1168, 2021.

[19] S. S. Chen, D. L. Donoho, and M. A. Saunders, "Atomic decomposition by basis pursuit," *SIAM Review*, vol. 43, no. 1, pp. 129–159, 2001.

[20] D. L. Donoho and J. Tanner, "Thresholds for the recovery of sparse solutions via L1 minimization," in *Proceedings of the 2006 40th Annual Conference on Information Sciences and Systems*, pp. 202–206, IEEE, Princeton, NJ, USA, 2006.

[21] M. Hyder and K. Mahata, "An approximate L0 norm minimization algorithm for compressed sensing," in *Proceedings of the 2009 IEEE International Conference on Acoustics, Speech and Signal Processing*, pp. 3365–3368, IEEE, Taipei, Taiwan, 2009.

[22] E. J. Candes and T. Tao, "Decoding by linear programming," *IEEE Transactions on Information Theory*, vol. 51, no. 12, pp. 4203–4215, 2005.

[23] S. Kumar, R. Vig, and P. Kapur, "Development of earthquake event detection technique based on STA/LTA algorithm for seismic alert system," *Journal of the Geological Society of India*, vol. 92, no. 6, pp. 679–686, 2018.

[24] Y. Vaezi and M. Van der Baan, "Comparison of the STA/LTA and power spectral density methods for microseismic event detection," *Geophysical Journal International*, vol. 203, no. 3, pp. 1896–1908, 2015.

[25] D. Wang, W. Zhang, X. Wang, and B. Sun, "Lamb-wave-based tomographic imaging techniques for hole-edge corrosion monitoring in plate structures," *Materials*, vol. 9, no. 11, p. 916, 2016.